Journal of Composite Materials 56 (2022) p. 1529-1540, DOI: 10.1177/00219983221074796

Compressive testing of thermoset composites reinforced with high-performance polymer fibres

Kathleen Schuurbiers[a], Larissa Gorbatikh[a], Yentl Swolfs*[a]
[a]Department of Materials Engineering, KU Leuven, Kasteelpark Arenberg 44 box 2450, Belgium
*Corresponding author: Y. Swolfs (yentl.swolfs@kuleuven.be), Tel.: +3216373616

Abstract

High-performance polymer fibres offer promising tensile and physical properties but are rarely used in structural composite applications due to their poor compressive performance. To better understand their performance inside a composite, unidirectional thermoset composites made with three types of polymer fibres were tested in shear-loaded compression. The results confirmed the poor compressive performance of the composites despite good fibre alignment, low porosity, and decent interfacial adhesion. Showing that the fibres collapse rather than microbuckle proves that the intrinsic fibre behaviour in compression is the key culprit. The developed finite element model predicted that the short gauge lengths required to avoid buckling lead to significant strain concentrations due to the grips. This causes the test to underestimate the compressive modulus, and potentially the rest of the compressive stress in the stress-strain diagram.

Keywords: Polymer fibres; Polymer-matrix composites; Compressive testing; Stress concentrations; Buckling.

1 Introduction

High-performance polymer fibres, such as aramid and ultrahigh molecular weight polyethylene fibres, combine excellent tensile stiffness and strength with a low density [1-3]. Some of these fibres even outperform standard carbon fibres in this respect [2]. Composites made with these fibres offer excellent impact resistance at low and high velocities [4, 5], and outstanding cutting, fire, and chemical resistance [1, 2]. These properties stem from their molecular structure, which typically consists of a molecular backbone with aromatic rings. These rigid rod molecules tend to show liquid crystallinity, which is a phase in between the liquid and solid phase. In this mesophase, the molecules can flow like a liquid, but they maintain crystal-like orientations. After spinning, the mesophase leads to fibrils with high orientation levels, but limited bonding between the fibrils [1, 2, 6]. This explains the low shear and off-axis properties of the fibres, which contribute to their cutting and impact resistance [5].

The poor bonding between the fibrils also limits the compressive performance [6, 7], which is why high-performance polymer fibres are rarely used in structural applications. In such applications, they are always used in combination with structural fibres like carbon fibres [3]. Significant research has been devoted to improving the bonding between the fibrils, either by developing new polymer chemistry [8] or altering existing polymer fibres [9, 10].

Generally speaking, compressive failure of composites can be triggered by three mechanisms [11]: microbuckling, fibre collapse and longitudinal cracking or splitting. Microbuckling occurs when the matrix provides insufficient support to the fibres. Fibre collapse occurs primarily for fibres that are weak in compression, such as polymer fibres. Longitudinal cracking or splitting is linked to interfacial debonding, and hence occurs in composites with a weak fibre/matrix bond or high void content. Kinking is sometimes considered to be a fourth mechanism, but it is actually the consequence of microbuckling or fibre collapse [11, 12].

The low compressive performance of polymer fibres is primarily based on single fibre test data, for which several methods have been devised. Elastica loop tests [7, 13, 14] and bending beam tests [15] both have a bending nature, and they assume that the compressive modulus is equal to the tensile modulus. This assumption is invalid for high-performance polymer fibres [13, 15], and leads to an overestimation of the fibre strength compared to tests at the composite level. In fibre recoil tests, the fibre strength is determined from the compressive snapback after tensile rupture [14]. The high wave propagation speed makes it difficult to observe the exact deformation mode (longitudinally, laterally or a combination of both). This prevents subsequent adjustment of the derivation of the compressive strength to the deformation mode, which differs from the fibre failure in a composite [14]. Finally, direct compression tests use very small gauge lengths of 200 to 500 µm to avoid Euler buckling of the single fibre, leading to highly non-uniform stress distributions caused by the grips [13, 15, 16]. All these methods are challenging to perform reliably and accurately. Even if such tests could be performed reliably and accurately, the question remains whether the measurements are relevant for the fibre behaviour inside a composite.

This paper uses the shear-loaded compression test to assess the compressive behaviour of thermoset composites reinforced with high-performance polymer fibres. It will establish whether this test method is an appropriate and reliable test methodology for such composites. The fibre alignment, void content and fibre-matrix adhesion are first characterised, as they can have a detrimental effect on the compressive performance [17-23]. The reliability of the test methodology is established by comparison against finite element model predictions.

2 Materials and methods

2.1 Materials

Yarns of three different fibre types were sourced: aramid, polyarylate (PAR) and polybenzobisoxazole (PBO) fibres. The aramid fibres were Twaron 2200 with a tensile modulus and strength of 110 GPa and 3300 MPa, respectively. The PAR fibres were Vectran HT with a tensile modulus and strength of 75 GPa and 3200 MPa. The PBO fibres were Zylon HM with a tensile modulus and strength of 270 GPa and 5800 MPa. All yarns had a similar linear density: 161, 167 and 164 tex, respectively.

A thermoset epoxy prepregging resin was sourced from Sicomin. This was a SiPreg SR8500 resin with a KTA313 amine-based hardener.

2.2 Manufacturing

Prepregs were manufactured using an in-house drum winder with the resin bath at room temperature. The resin and hardener were mixed in a ratio of 100/21 by weight, after which the mixture was degassed for 15 minutes. Prepreg sheets of 300x300 mm were cut and 35 sheets were stacked together and placed in an autoclave. The samples were cured at 60°C for 240 min and post-cured at 120°C for 120 min. A vacuum pressure of 0.65-0.7 bar was applied throughout the process, whereas the nitrogen overpressure was toggled on once the curing temperature of 60°C was attained. This led to a nominal panel thickness of 8 mm, 7.3 mm and 8.1 mm for aramid, PAR and PBO, respectively. Optical microscopy and image analysis were used to calculate the fibre volume fraction to be 50%, 51% and 52%, respectively.

2.3 Microdroplet tests

Microdroplets tests were performed to evaluate the interfacial adhesion. SR8500/KTA313 epoxy droplets were added to the fibres and cured in an oven at atmospheric pressure using the same temperature cycle as in the autoclave. After conditioning the fibres for at least 24 hours, the droplet diameter and embedded length were measured using optical microscopy. The specimens were then tested on a mini tensile testing machine with a 5 N load cell. Two straight knives were placed on top of the droplet, and the fibre was pulled out (see Figure 1). The displacement rate was set to 0.5 mm/min. The interfacial shear strength was obtained by dividing the maximum force by the surface area of the droplet that was in contact with the fibre. The number of specimens tested was 11, 8 and 7 for aramid/epoxy, PAR/epoxy and PBO/epoxy, respectively.

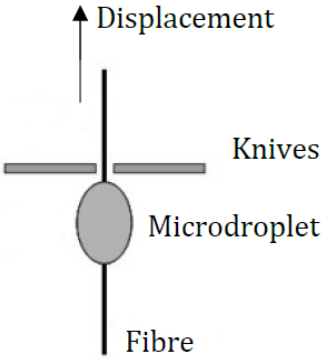

Figure 1: Schematic of the microdroplet setup.

2.4 Microcomputed tomography

A GE NanoTom device with a molybdenum target was used to perform one X-ray microcomputed tomography scan on each of the three composites. The voltage was 70 kV, 70 kV and 56 kV for aramid/epoxy, PAR/epoxy, and PBO/epoxy specimens, respectively, whereas the current was 370 µA, 340 µA and 255 µA, respectively. The specimens were 1 mm x 1 mm x 10 mm. A total of 1200 projections were taken with an exposure time of 750 ms for aramid/epoxy and PAR/epoxy specimens and 500 ms for PBO/epoxy specimens. The voxel size was 1.2 µm for aramid/epoxy and PAR/epoxy, and 1.8 µm for PBO/epoxy. Since the fibre/matrix contrast was insufficient for automatic segmentation (see Figure 2), at least 30 fibre paths were tracked and measured manually. This was done in-plane as well as out-of-plane, and the standard deviation on all the measurement was reported.

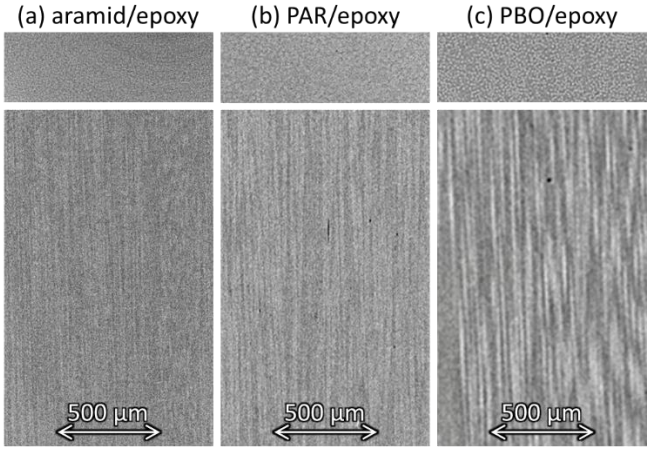

Figure 2: Two orthogonal views for the computed tomography scans: (a) aramid/epoxy, (b) PAR/epoxy, and (c) PBO/epoxy

2.5 Microscopy

Optical microscopy images were taken perpendicular to the fibre direction to measure the fibre volume fraction. For aramid/epoxy and PBO/epoxy, this was done at a 50x magnification with an analysed area of 50x50 µm. For PAR/epoxy, the magnification was reduced to 10x and the analysed area was increased to 700x1000 µm. ImageJ was used to threshold at least 40 images per fibre type. Stereomicroscopy was performed on failed compression specimens. A Philips scanning electron microscope (SEM) XL30 FEG was used to analyse the fracture surface of the compression. The compression specimens were ground and polished before they were coated with 5 nm of platinum.

2.6 Compression tests

Shear-loaded compression tests were performed according to ASTM D3410 on an Instron 5985 with a 250 kN load cell. The details of the test fixture are described in this standard. The results reported here were all for a 5 mm gauge length, even though initial tests were performed at longer gauge lengths. The specimen thicknesses were equal to the panel thicknesses mentioned in section 2.2 Manufacturing, whereas the nominal specimen width was 7 mm. Double-sided sanding paper was used to prevent or limit slippage in the grips. The displacement rate was set to 0.5 mm/min. Due to machine compliance, this corresponded roughly to a strain rate of 0.4%/min. At least 6 specimens were tested for each fibre type.

Speckle patterns were applied to the front and back of the specimen (see Figure 3), and images were taken on both sides every 1s. Digital image correlation was performed afterwards using Limess Vic2D-2009 from Correlated Solutions with a subset size of 21 pixels (see Figure 3) and a step size of 5 pixels. The longitudinal strain was averaged over a region with a width and height of 7 mm and 3 mm, respectively (see Figure 3). The compressive modulus was determined between 0.05% and 0.1% of strain to avoid the non-linear regime. The presence of buckling was determined using the percent bending equation provided by the ASTM standard. This equation was not only evaluated at the back and front, but also on the left and right of the specimen to monitor lateral buckling.

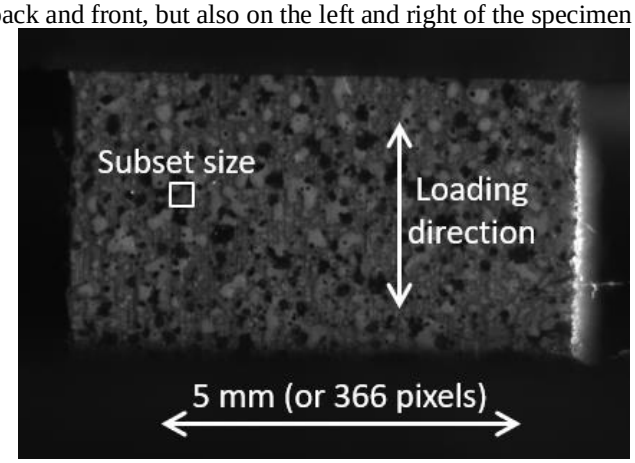

Figure 3: Illustration of the DIC speckle pattern, subset size and field of view.

3 Experiment results

3.1 Quality control

The optical microscopy images (see Figure 4) prove that all three composites are of high quality, with limited porosities overall and without any large voids. The aramid/epoxy and PBO/epoxy composites reveal a banded structure, which reflects the ply boundaries. Such ply boundaries are absent in the PAR/epoxy composite.

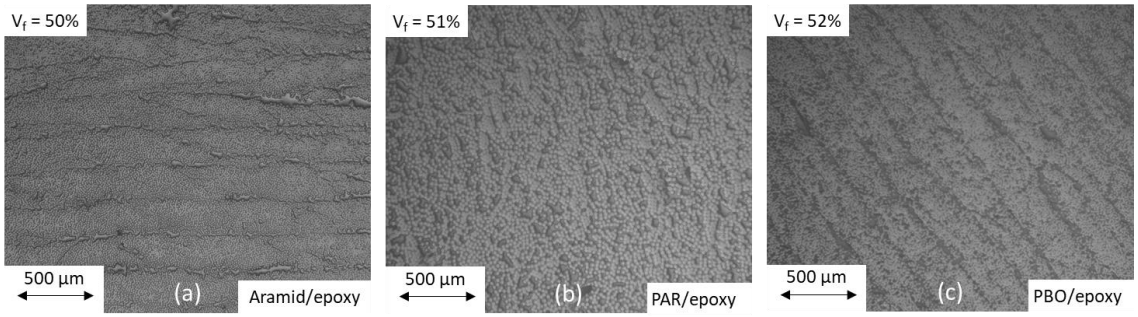

Figure 4: Optical microscopy of all three composites: (a) aramid/epoxy, (b) PAR/epoxy and (c) PBO/epoxy.

A remarkable feature found in all three composites is the presence of high V_f regions (see Figure 5). Locally, the V_f is well above 90.7%, which is the theoretical limit for a hexagonal packing of circles. The same feature was observed by Huang et al. [24], who reported global fibre volume fractions above 90%. These fibres are compliant in the transverse direction, allowing them to change their shape under the autoclave pressure.

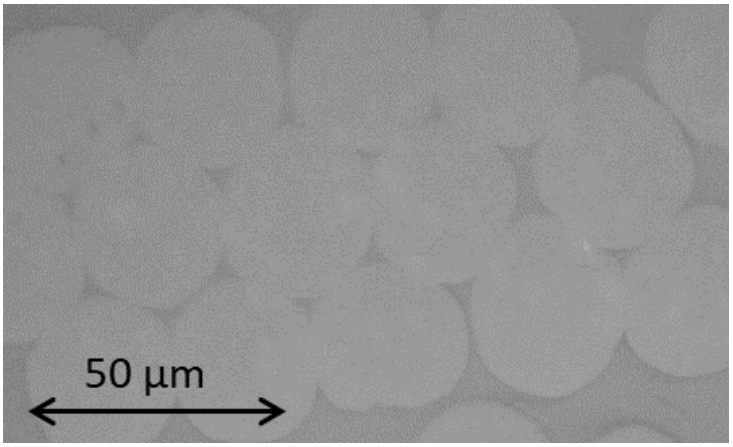

Figure 5: Close up of a high fibre volume fraction region in PAR/epoxy, with the PAR fibres in the lighter grey colour. The other two composites showed similar regions.

The fibre misalignment was measured manually from the microCT data. The values in Table 1 illustrate that the fibres were well aligned. Inspection of the microCT volumes provided further evidence of the low porosity content seen in the optical microscopy images (see Figure 4).

Table 1: Fibre misalignment in all three composites, measured manually from the microCT data. The 3D misalignment was estimated based on Pythagoras' theorem. The contrast between aramid fibres and epoxy was too low to obtain reliable measurements.

	In-plane misalignment	Out-of-plane misalignment	Estimated maximum 3D misorientation
Aramid/epoxy	-	-	-
PAR/epoxy	1.41°	2.91°	3.23°
PBO/epoxy	1.12°	2.44°	2.69°

3.2 Interfacial characterisation

Table 2 reports the results of the microdroplet tests for all three composites. Scanning electron microscopy images confirmed that the fractures for aramid/epoxy and PBO/epoxy happened in an adhesive manner: the droplet was pulled off the fibre without damaging the fibre and without leaving behind resin on the fibre (see Figure 6a and c). For PAR/epoxy, the fracture seems to have occurred within the fibre (see Figure 6b), implying that the measured value is a lower limit for interfacial shear strength.

Table 2: Interfacial shear strength of the three composites, as calculated from microdroplet test results.

	Aramid/epoxy	PAR/epoxy	PBO/epoxy
Interfacial shear strength [MPa]	27.1 ± 4.2	28.0 ± 0.5	37.2 ± 1.9

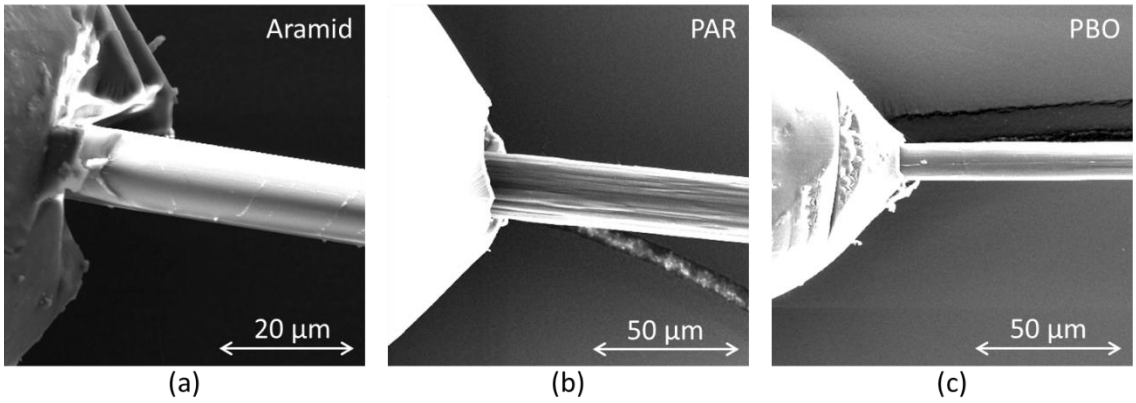

Figure 6: Scanning electron microscopy images of microdroplet specimens after the test: (a) aramid/epoxy showing a clean, adhesive fracture, (b) PAR/epoxy showing a damage fibre surface, and (c) PBO/epoxy showing a clean, adhesive fracture.

The measured values are reasonably high compared to other microdroplet tests reported in the literature: 24 MPa for aramid/epoxy [25], 4.7 MPa [26], 5.5 MPa [27] and 11.3 MPa [28] for untreated PBO/epoxy and 19 MPa for untreated PAR/epoxy [29]. Higher values were found in single fibre pull-out tests: Mäder et al. [30] measured 39-55 MPa for PBO/epoxy and Zhandarov and Mäder [31] measured 42-50 MPa for two aramid/epoxy systems. These discrepancies are not surprising, given the well-established difficulties in comparing different interfacial characterisation methods [32].

3.3 Compression tests

Prior to the first tests, the Engesser-derived buckling formula in the ASTM standard [33] and Saint-Venant's principle [34] were used to calculate the minimum and maximum gauge length. The obtained values ranged between 51 and 88 mm. When testing at these gauge lengths, however, buckling was detected in all cases. This is because the Engesser formula assumes a linear elastic material, and these materials are not linearly elastic. The gauge length was therefore reduced until buckling was avoided. At a 10 mm gauge length, buckling still occurred, but at 5 mm it did not occur anymore. This gauge length satisfies the limit imposed by the Engesser formula but violates Saint-Venant's principle. This implies that the stress concentrations from the grips cannot be ignored, a feature that will be analysed in section "4.3 Strain concentration predictions".

Figure 7 reveals the compressive stress-strain diagrams for PAR/epoxy and PBO/epoxy. The results for aramid-epoxy are not shown here, as the specimens slipped in the grips before yielding started. We believe this is due to the higher compressive strength of aramid/epoxy compared to the other two composites. The compressive moduli of aramid/epoxy, PAR/epoxy and PBO/epoxy were measured to be 41 $\pm$ 4 GPa, 26 $\pm$ 2 GPa and 64 $\pm$ 8 GPa, respectively. PAR/epoxy and PBO/epoxy both show early onset of yielding slightly below or above 100 MPa. The plastic behaviour explains why the samples buckled at the larger gauge lengths, as the Engesser formula assumes linear elastic materials.

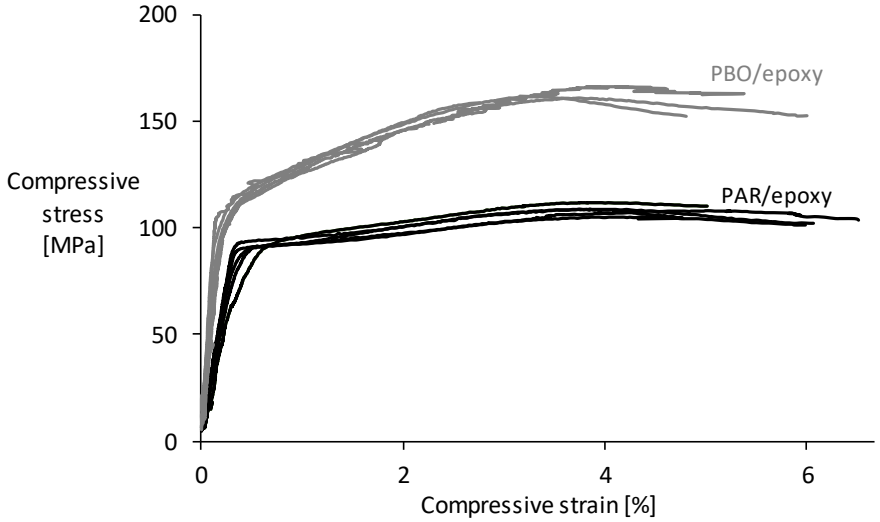

Figure 7: The compressive stress-strain diagrams of PAR/epoxy and PBO/epoxy composites, tested at a gauge length of 5 mm.

Since the aramid/epoxy samples slipped in the grips, the compressive failure surface could not be analysed. The failed PAR/epoxy and PBO/epoxy specimens showed kink bands at an angle of 34 $\pm$ 1° and 31 $\pm$ 3°, respectively. Figure 8a presents an example of such a kink band for PBO/epoxy. Rather than breaking at the edges of the kink bands like carbon/epoxy would, the polymer fibres bend or shear off.

Kink bands also formed on a smaller scale, namely within the fibres (see Figure 8b). On this scale, the kink band angle was 25 ± 1° for PAR/epoxy. These fibre-level kink bands indicate that, in contrast with most carbon and glass fibre composites, the fibres collapsed rather than micro-buckled. For PBO/epoxy, these kink bands could not be observed due to post-mortem damage. However, since the failure of PBO/epoxy was generally very similar to PAR/epoxy, it is a reasonable assumption that PBO fibres failed in the same manner as PAR fibres.

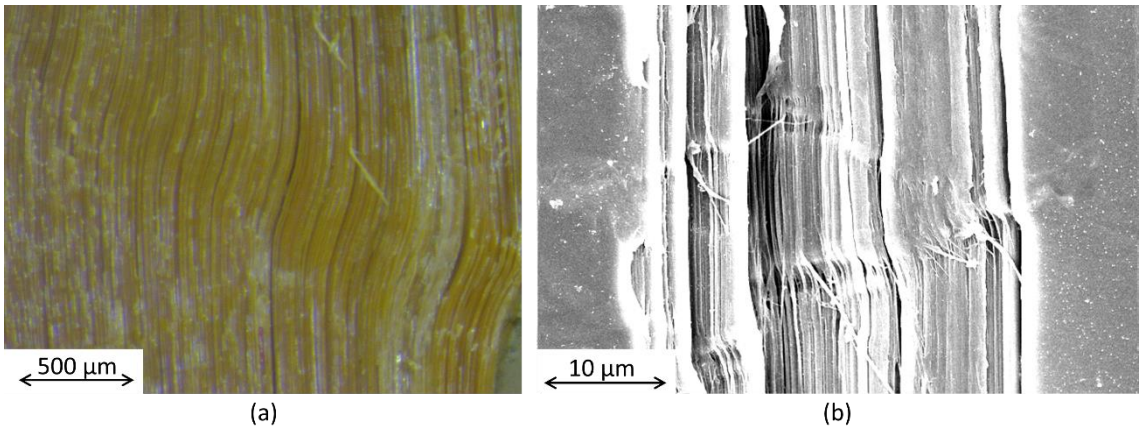

Figure 8: Microscopy images of the compressive failure: (a) stereomicroscopy image of a kink band in PBO/epoxy, and (b) scanning electron microscopy image of the kink band inside a PAR fibre.

4 Model predictions

4.1 Model description

To identify the critical buckling length for materials that are not linear elastic materials, we cannot use the Engesser buckling formula. We therefore developed finite element models in Abaqus 2016 to predict the buckling gauge length and the strain concentrations for all three composites. Both models assumed that the material was homogeneous and transversely isotropic with the engineering constants listed in Table 3. E_z was measured from the compression tests, without the correction factor described later on in section "4.3 Strain concentration predictions". All other values were estimated from the literature [24, 35-39] combined with micromechanical predictions and the measured fibre volume fractions (see Figure 4).

Table 3: Engineering constants of the three composites, with the z-direction being the fibre direction. The E_z values were taken from the experiments after normalisation to a 50% fibre volume fraction using the linear rule-of-mixtures.

Material	$E_x = E_y$ [GPa]	E_z [GPa]	ν_{xy} [-]	$\nu_{xz} = \nu_{yz}$ [-]	G_{xy} [GPa]	$G_{xz} = G_{yz}$ [MPa]
Aramid/epoxy	2.7	40.9	0.44	0.0046	1.54	1.50
PAR/epoxy	1.2	26.3	0.52	0.0046	1.50	1.13
PBO/epoxy	2.7	61.7	0.60	0.0046	1.50	1.00

The buckling model used linear brick elements C3D8R with hourglass control. The elements were all cubic with 1 mm sides, as further mesh refinements did not alter the results significantly. The width and thickness of the buckling model corresponded to the dimensions in the experiments (see sections 2.2 Manufacturing and 2.6 Compression tests). The length was progressively decreased from 50 mm down to 5 mm. Pinned-pinned boundary conditions (see Figure 9a) were applied to the top and bottom surface of the sample, as they are considered to be more appropriate than fixed-fixed boundary conditions (see Figure 9b) [34]. In practice, the boundary conditions lie somewhere in between these two idealised cases, but fixed-fixed conditions will become more suitable when the material deviates more from linearity. The non-linear compressive behaviour of the materials was incorporated by iteratively replacing the compressive modulus by the tangent modulus at a given stress level, as suggested by Ylinen [40] and Stowell [41]. This stress level was increased in steps of 1 MPa, until just before the compressive strength was achieved. The stress level at which the corresponding tangent modulus caused buckling, was considered to be the buckling stress. The buckling gauge length is the smallest gauge length at which the buckling stress is smaller than the stress level for the tangent modulus calculation.

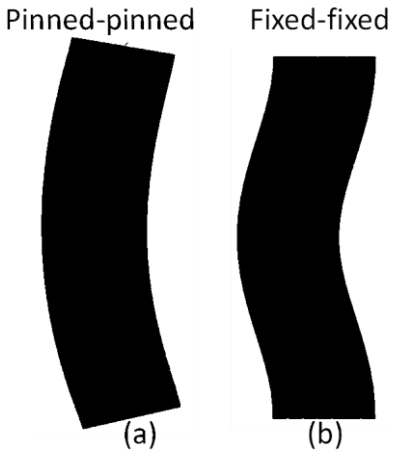

Figure 9: Comparison of the buckling mode for (a) pinned-pinned and (b) fixed-fixed end conditions.

The finite element model for strain concentrations used linear brick elements C3D8R. The elements near the grips were 195 x 195 x 50 µm with the smallest dimension in the Z-direction (see Figure 10). The mesh was gradually coarsened away from the grips, and further mesh refinements had only minor effects on the results. In contrast with the buckling model, this model also incorporated the steel grips (see Figure 10). A pressure of 2 MPa is applied to the grips for the 200 mm gauge length models, with a friction coefficient of 0.7 between the steel and the specimen to represent the presence of double-sided sanding paper [42, 43]. For the 5 mm gauge length models, the applied pressure was reduced to 0.01 MPa, as these simulations ran only in the linear elastic regime. Due to the nature of the grips in the experiments, the exact pressure level remains unknown. The augmented Lagrange constraint enforcement method was used to simulate the contact behaviour. Symmetry was exploited to reduce the model size to 1/8 of the actual problem (see Figure 10). The 200 mm gauge length models were run with linear elastic as well as elastoplastic material properties to assess the influence of the plasticity. The elastoplastic behaviour was taken from the stress-strain diagrams in Figure 7 and implemented using the standard Abaqus plasticity model, which uses associated plastic flow and isotropic hardening.

The models were first run at 200 mm gauge length to calculate the strain concentration decay length, which was defined as the length at which the strain concentrations are below 1%. Further away, the strain concentrations are so low that the strain field can be considered uniform. A displacement of 3 mm was applied to the right-hand side of the grip in Figure 10, which led to an equilibrium strain close to 1%. This was well into the plastic regime (see Figure 7). Next, the models were run at 5 mm gauge length to simulate the experimental setup. A displacement of 2.5 µm was applied to the right-hand side of the grip in Figure 10. Taking into account the symmetry and the 50 mm long grips, the models represented a total sample length of 300 mm or 105 mm, respectively (see Figure 10). The models took into account the elastoplastic response measured from the experiments (see Figure 7).

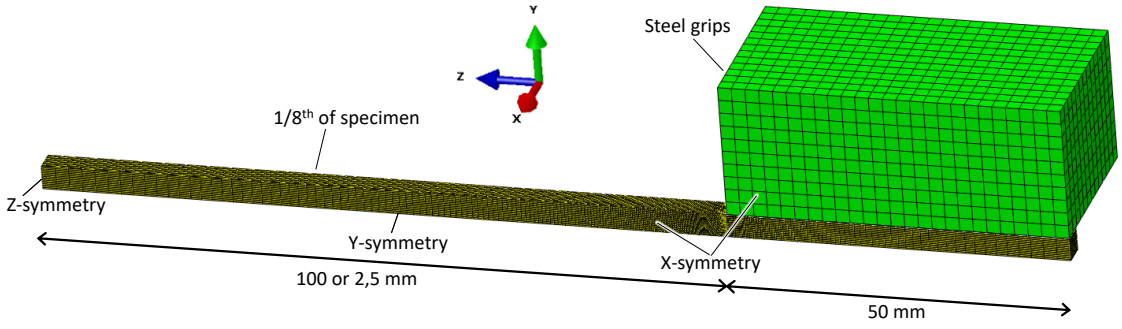

Figure 10: 3D view of the models with the steel grips and sample to predict strain concentrations.

4.2 Buckling predictions

An iterative procedure was set up to identify the critical buckling gauge length (see Figure 11). A gradual increase in the stress level in the model led to a decrease in the tangent modulus, as identified from the local slope on the experimental compressive stress-strain diagram. This corresponds to moving to the left in Figure 11. At the same time, the decreasing tangent modulus lowered the buckling stress. The models revealed that the shortest gauge length for which both lines intersected was 12 mm for both PAR/epoxy and PBO/epoxy. This length was hence the predicted buckling gauge length.

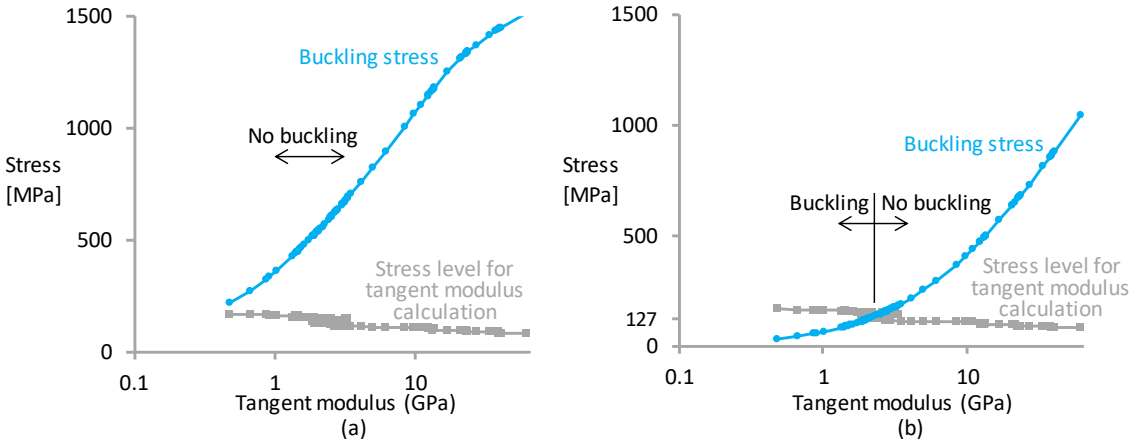

Figure 11: The iterative procedure for finding the buckling gauge length: (a) for a 10 mm PBO/epoxy model which will not buckle prior to reaching its compressive strength, and (b) for a 25 mm PBO/epoxy model which will buckle at 127 MPa.

4.3 Strain concentration predictions

The model was first used to predict the strain concentration decay length, as defined in section "4.1 Model description". This was done for both elastic and elastoplastic material properties. The evolution of two different types of longitudinal strain ε_{zz} were analysed along the length of the specimen: the maximum longitudinal strain over the entire cross-section and the average longitudinal strain on the front and the back. The average longitudinal strain on front and back is the most relevant parameter, as that is where the strains are being measured experimentally.

The results are summarised in Table 4. The gauge length should be more than twice the strain concentration decay length to allow reliable measurements. The results hence clearly illustrate that the experimentally used gauge length of 5 mm is not large enough to achieve a uniform strain region in the middle of the specimen. The yielding of the material significantly contributes to shortening the decay length. It is noteworthy that PBO/epoxy has the longest decay length in the elastic case, but the shortest decay length in the elastoplastic case. The longer decay length in the elastic case is attributed to the larger anisotropy of this composite, as seen from its E_3/G_{13} ratio (see Table 3). The decay length trends in the plastic case are more difficult to explain, as it depends on the strain-dependent E_3/G_{13} ratio, which is different throughout the modelled specimen.

Table 4: Summary of the strain concentration decay length. The elastoplastic results for aramid/epoxy are not included, as the required compressive stress-strain diagrams could not be measured reliably.

		Strain concentration decay length (mm)	
		Maximum strain	Front-back strain
Aramid/epoxy	Elastic	15.5	10.5
	Elastoplastic	-	-
PAR/epoxy	Elastic	15.8	7.2
	Elastoplastic	12.8	11.0
PBO/epoxy	Elastic	27.9	26.4
	Elastoplastic	11.0	3.4

Next, the models were run for a 5 mm gauge length with only the elastic material properties. This hence represents the experimental scenario at the strain levels where the modulus was measured. For these models, the average stress over the cross-section was divided by the average of the longitudinal strains at the front and back of the specimen. The result of this calculation should be the elastic modulus that was used as input. However, due to the strain concentrations near the grips, this value deviates from the input value. The obtained modulus was 12.2%, 5.4% and 10.2% lower than the input modulus for aramid/epoxy, PAR/epoxy, and PBO/epoxy, respectively. These values provide an estimate for the underestimation of the modulus measured in the experiments.

5 Discussion

In the experiments, the practical buckling gauge length was found to lie between 5 and 10 mm for PAR/epoxy and PBO/epoxy, which is a bit lower than the buckling model predicted. Two important caveats should be highlighted. Firstly, some of the engineering constants in Table 3 are not known very accurately. As the compressive stresses are built up through shear stresses, knowing the shear components accurately could have a significant influence on the calculations. Secondly, the calculations were based on the measured stress-strain diagrams without considering the correction suggested in section "4.3 Strain concentration predictions". Since the actual stiffness is

slightly higher, the overprediction of the buckling gauge length could be expected to be even more severe. However, the effect on the entire stress-strain diagram remains unknown.

Based on the presented measurements and fibre volume fraction, the compressive fibre modulus and strength can be back-calculated and compared to those found in the literature. The modulus and strength back-calculations were performed based on linear and bilinear rule-of-mixtures, respectively. Figure 12 presents the fibre compressive modulus data. The majority of the data points are below the present measurements. For aramid, three crosses indicate the data measured in a bending beam test. This type of test has several drawbacks. Firstly, the bending beam test involves gluing the fibre onto a thick beam, which is then deflected in bending. The gluing creates a composite-like structure, making the test similar to a composite compression test. Secondly, the fibre is pre-strained, which partially offsets the bending loads. This can lead to erroneous results, as the tensile moduli of these polymer fibres differ from their compressive moduli. For PAR, only two data points were found [44], but the source did not mention the test method. For PBO, one data point is above the present measurements, and this was again measured in a bending beam test.

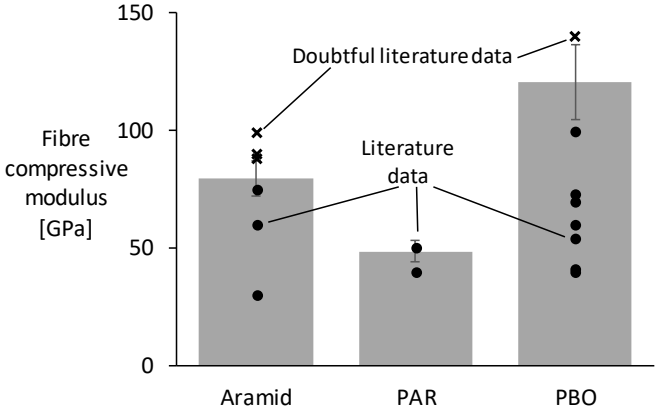

Figure 12: Back-calculated fibre compressive modulus in grey bars compared against literature data in the black markers [15, 16, 44-46]. The reported moduli are the measured ones, without applying the potential correction based on the finite element models that was described in section "4.3 Strain concentration predictions".

Figure 13 present the fibre compressive strength data. Nearly all the data reported in the literature are higher than the present measurements. The majority of this data was, however, measured on individual fibres, which is known to overestimate the compressive strength [16].

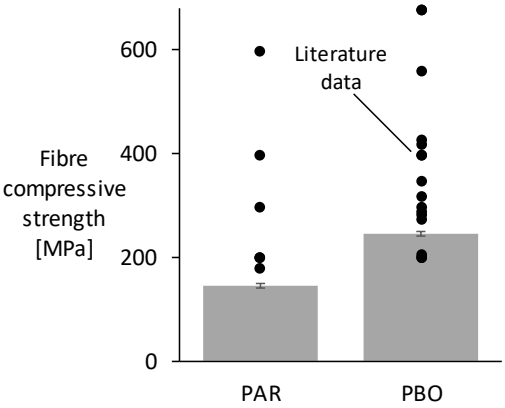

Figure 13: Back-calculated fibre compressive strength in grey bars compared against literature in black dots [13, 15, 16, 44, 46-58].

The present experimental campaign on unidirectional composites indicated that (1) the fibres were well aligned (see Table 1), (2) the interfacial adhesion was reasonably good (see Table 2) and (3) the composites were well impregnated and nearly void-free. This combination caused the fibres to collapse (see Figure 8) rather than to microbuckle like carbon and glass fibre composites. Fibre collapse is an indication that further improvements in fibre alignment, interfacial adhesion and matrix yield stress are unlikely to result in improved compressive performance of the composites.

Given the low compressive strength of the high-performance polymer fibres and their composites, the question is whether anything else can be improved for broadening their application potential. Many structural applications will be subjected to bending, which inflicts compressive stresses. Two potential strategies are proposed for addressing this. The first strategy involves improving the polymer chemistry of the fibres to create stronger intermolecular bonds. This can be realised through the development of new polymer fibres or through improving the existing ones [8-10]. This strategy has already been actively pursued by many researchers, and for example led to the development of the polyhydroquinone-diimidazopyridine (PIPD) fibre [1, 2]. The second strategy is to exploit

fibre-hybridisation. By combining a compressively weak fibre with a structural fibre, such as glass or carbon fibre, the compressive loads can be taken up by the structural fibre. This could lead to significant synergetic effects, especially when the fibres are well dispersed [3, 59]. Fibre-hybridisation of polymer fibres has received limited attention in the literature, but is already extensively explored in sports applications [3].

It is clear that properly testing high-performance polymer fibres and their composites in compression is a challenging task. The presented results indicate that the properties measured on individual fibres are not representative for their properties inside a composite. It therefore becomes vital to perform a composite-level test. The poor compressive performance and significant anisotropy of high-performance polymer fibres, however, hamper the accuracy of the shear-loaded compression test. The end-loaded compression test (ASTM D695) will be less sensitive to the strain concentrations issue described in section "4.3 Strain concentration predictions". However, the low compressive performance of high-performance polymer fibres is likely to trigger failure at the ends. A sandwich beam method (ASTM D5467) can help to avoid the strain concentrations and buckling issues, but the difference between tensile and compressive moduli will hamper its interpretation and accuracy. Essentially, this method would require a priori knowledge of the compressive and tensile stress-strain diagrams, which goes against the point of the test. A slightly better approach than the shear-loaded compression test therefore may be the combined loaded compression test (ASTM D6641). However, this test would still require very short gauge lengths to avoid buckling, although the stress concentration issues are likely to be less severe. The slipping issue we experienced with aramid-epoxy would likely caused the combined-loaded test to be primarily end-loaded, and hence trigger failure at the ends. The thickness and width could be increased further, but the 7-8 mm used here is already very thick. Even thicker composites may face curing difficulties due to excessive exothermal reactions causing resin degradation [60].

6 Conclusions

The shear-loaded compression test was used to measure the compressive stress-strain diagrams of epoxy-based composites reinforced with high-performance polymer fibres. The fibres were well aligned, the composites had a lower porosity content and showed decent interfacial strength. While the aramid fibre composite could not be tested until failure, the PAR and PBO fibre composites showed early onset of yielding and a low compressive strength. The failure was triggered by fibre collapse, indicating that the inherent weakness of the fibres caused compressive failure. To avoid buckling, the test had to be performed at short gauge lengths where strain concentrations from the grips were unavoidable. A finite element model was developed to assess the influence of this strain concentration. The model revealed that the strain concentrations led to an underestimation of the compressive modulus by 12.2%, 5.4% and 10.2% for aramid/epoxy, PAR/epoxy, and PBO/epoxy, respectively. This measurement error likely reduced once yielding started, which lowered the strain concentrations. Combining shear-loaded (or combined-loaded compression) testing with finite element modelling is suggested here as the solution for reliable compressive testing of composites with high-performance polymer fibres. It would also be helpful to perform interrupted compression tests to observe more carefully how the micromechanisms develop as a function of applied strain.

Future efforts should focus on fibre-hybridisation as a powerful strategy to overcome the poor compressive performance of the high-performance polymer fibre composites and broaden their application potential. In addition, developing micromechanical models that include fibre failure would help in better understanding the failure mechanisms, and improving performance.

7 Acknowledgments

YS acknowledges the support of FWO Flanders for his postdoctoral fellowship.

8 References

1. Chae HG and Kumar S. Rigid-rod polymeric fibers. *J Appl Polym Sci*. 2006; 100: 791-802.
2. Afshari M, Sikkema DJ, Lee K and Bogle M. High performance fibers based on rigid and flexible polymers. *Polym Rev*. 2008; 48: 230-274.
3. Swolfs Y, Verpoest I and Gorbatikh L. Recent advances in fibre-hybrid composites: materials selection, opportunities and applications. *Int Mater Rev*. 2019; 64: 181-215.
4. Park R and Jang JS. Impact behavior of aramid fiber glass fiber hybrid composite: Evaluation of four-layer hybrid composites. *J Mater Sci*. 2001; 36: 2359-2367.
5. Morye SS, Hine PJ, Duckett RA, Carr DJ and Ward IM. Modelling of the energy absorption by polymer composites upon ballistic impact. *Compos Sci Technol*. 2000; 60: 2631-2642.
6. Andres Leal A, Deitzel JM, McKnight SH and Gillespie Jr JW. Interfacial behavior of high performance organic fibers. *Polymer*. 2009; 50: 1228-1235.

7. Leal AA, Deitzel JM, McKnight SH and Gillespie Jr JW. Effect of hydrogen bonding and moisture cycling on the compressive performance of poly-pyridobisimidazole (M5) fiber. *Polymer*. 2009; 50: 2900-2905.
8. Sikkema DJ. Design, synthesis and properties of a novel rigid rod polymer, PIPD or 'M5': high modulus and tenacity fibres with substantial compressive strength. *Polymer*. 1998; 39: 5981-5986.
9. Lorenzo-Villafranca E, Tamargo-Martinez K, Molina-Aldareguia JM, et al. Influence of Plasma Surface Treatments on Kink Band Formation in PBO Fibers During Compression. *J Appl Polym Sci*. 2012; 123: 2052-2063.
10. Wang J, Chen P, Li H, et al. Surface characteristic of poly(p-phenylene terephthalamide) fibers with oxygen plasma treatment. *Surf Interface Anal*. 2008; 40: 1299-1303.
11. Schultheisz CR and Waas AM. Compressive failure of composites, part I: Testing and micromechanical theories. *Progress in Aerospace Sciences*. 1996; 32: 1-42.
12. Wang Y, Burnett TL, Chai Y, Soutis C, Hogg PJ and Withers PJ. X-ray computed tomography study of kink bands in unidirectional composites. *Compos Struct*. 2017; 160: 917-924.
13. Leal AA, Deitzel JM and John W. Gillespie J. Compressive Strength Analysis for High Performance Fibers with Different Modulus in Tension and Compression. *J Compos Mater*. 2009; 43: 661-674.
14. Furuyama M, Higuchi M, Kubomura K, Sunago H, Jiang H and Kumar S. Compressive properties of single-filament carbon fibres. *J Mater Sci*. 1993; 28: 1611-1616.
15. Kumar S, Kozey V, Mehta V and Hu X. Study of the compression behavior of high performance fibers. 1994.
16. Fawaz SA, Palazotto AN and Wang C-S. Compressive Properties of High Performance Polymeric Fibers. Ohio, USA: Air Force Wright Aeronautical Laboratories, 1989.
17. Yurgartis SW. Measurement of small angle fiber misalignments in continuous fiber composites. *Compos Sci Technol*. 1987; 30: 279-293.
18. Wisnom MR. The effect of fibre misalignment on the compressive strength of unidirectional carbon fibre/epoxy. *Composites*. 1990; 21: 403-407.
19. Daniel IM and Hsiao HM. Is there a thickness effect on compressive strength of unnotched composite laminates? *Int J Fract*. 1999; 95: 143-158.
20. Hancox NL. The compression strength of unidirectional carbon fibre reinforced plastic. *J Mater Sci*. 1975; 10: 234-242.
21. Madhukar MS and Drzal LT. Fiber-Matrix Adhesion and Its Effect on Composite Mechanical Properties. III. Longitudinal (0°) Compressive Properties of Graphite/Epoxy Composites. *J Compos Mater*. 1992; 26: 310-333.
22. Bazhenov SL, Kuperman AM, Zelenskii ES and Berlin AA. Compression failure of unidirectional glass-fibre-reinforced plastics. *Compos Sci Technol*. 1992; 45: 201-208.
23. Liebig WV, Viets C, Schulte K and Fiedler B. Influence of voids on the compressive failure behaviour of fibre-reinforced composites. *Compos Sci Technol*. 2015; 117: 225-233.
24. Huang YK, Frings PH and Hennes E. Mechanical properties of Zylon/epoxy composite. *Composites Part B-Engineering*. 2002; 33: 109-115.
25. Li J and Caichilan CL. The interfacial shear strength of Kevlar fiber/epoxy composite measured by the microdroplet test. *Materialwiss Werkstofftech*. 2010; 41: 119-121.
26. Liu R, Han Z, Li W, Li X and Zhuang Q. Improvement of the interfacial shear strength of poly(p-phenylene benzobisoxazole) fiber/epoxy resin composite via a novel surface coating agent. *Polym Compos*. 2016; 37: 1198-1205.
27. Sugihara H and Jones FR. Promoting the adhesion of high-performance polymer fibers using functional plasma polymer coatings. *Polym Compos*. 2009; 30: 318-327.
28. Qian J, Wu J, Liu X, Zhuang Q and Han Z. Improvement of interfacial shear strengths of polybenzobisoxazole fiber/epoxy resin composite by n-TiO2 coating. *J Appl Polym Sci*. 2012; 127: 2990-2995.

29. Zeng J and Netravali AN. Effects of XeCl excimer laser treatment of Vectran® fibers and their adhesion to epoxy resin. *J Adhes Sci Technol*. 2006; 20: 387-409.
30. Mäder E, Melcher S, Liu JW, et al. Adhesion of PBO fiber in epoxy composites. *J Mater Sci*. 2007; 42: 8047-8052.
31. Zhandarov S and Mäder E. Characterization of fiber/matrix interface strength: applicability of different tests, approaches and parameters. *Compos Sci Technol*. 2005; 65: 149-160.
32. Teklal F, Djebbar A, Allaoui S, Hivet G, Joliff Y and Kacimi B. A review of analytical models to describe pull-out behavior – Fiber/matrix adhesion. *Compos Struct*. 2018; 201: 791-815.
33. ASTM D3410-03 -

Standard Test Method for Compressive properties of polymer matrix composite materials with unsupported gage section by shear loading. Philadelphia, USA: ASTM, 2003.
34. Bogetti TA, Gillespie JW and Pipes RB. Evaluation of the IITRI compression test method for stiffness and strength determination. *Compos Sci Technol*. 1988; 32: 57-76.
35. Yamashita Y, Kawabata S, Minami H, Okada S and Tanaka A. Fatigue Property of PBO Fiber. *(Published on-line at citeseerxistpsuedu)*. 2018.
36. Ward IM and Sweeney J. *Mechanical properties of solid polymers*. 3rd ed. Chichester, United Kingdom: John Wiley & Sons, 2012.
37. Hine PJ and Ward IM. Measuring the elastic properties of high-modulus fibres. *J Mater Sci*. 1996; 31: 371-379.
38. Pindera M-J, Gurdal Z, Herakovich CT, Hidde JS and Starbuck JM. Mechanical Response of Aramid/Epoxy under Tensile, Compressive and Shear Loading. *J Reinf Plast Compos*. 1989; 8: 410-420.
39. Kawabata S, Sera M, Kotani T and Katsuma K. Anisotropic Mechanical Properties of Advanced High Performance Fibers Obtained by a Single Fiber Testing System. In: Miravete A, (ed.). *9th International Conference on Composite Materials*. Madrid, Spain: Woodhead Publishing Limited, 1993, p. 671-677.
40. Ylinen A. A method for determining the buckling stress and the required cross-sectional area for centrally loaded straight columns in elastic and inelastic range. *Publ Int Assoc Bridge and Structural Engineering*. 1956; 16: 529-550.
41. Stowell EZ. A unified theory of plastic buckling of columns and plates. Virginia, USA: NASA Langley, 1948.
42. Zhao G, Hussainova I, Antonov M, Wang Q and Wang T. Friction and wear of fiber reinforced polyimide composites. *Wear*. 2013; 301: 122-129.
43. Cheng B and Kortschot M. A Study of the Friction Coefficients of Unidirectional and Woven Carbon Fibre/Epoxy Composites. *Polymers & Polymer Composites*. 2016; 24: 255-263.
44. Hoshiro H, Endo R and Sloan FE. Vectran®: Super fiber from the thermotropic crystals of rigid-rod polymer. In: Technology SoFS, (ed.). *High-Performance and Speciality Fibers*. Tokyo, Japan: Springer Japan, 2016.
45. Andres Leal A, Deitzel JM and Gillespie Jr JW. Assessment of compressive properties of high performance organic fibers. *Compos Sci Technol*. 2007; 67: 2786-2794.
46. McGarry FJ and Moalli JE. Mechanical behaviour of rigid rod polymer fibres: 1. Measurement of axial compressive and transverse tensile properties. *Polymer*. 1991; 32: 1811-1815.
47. Adams WW and Eby RK. High-Performance Polymer Fibers. *MRS Bull*. 2013; 12: 22-26.
48. Technical data sheet of Zylon PBO fiber. In: Ltd. TC, (ed.). Osaka, Japan2005.
49. Kumar S and Helminiak TE. Compressive Strength of high Performance Fibers. *MRS Proceedings*. 2011; 134: 363-374.

50. Wang CS, Bai SJ and Rice BP. Axial compressive strengths of high-performance fibers by tensile-recoil technique. *Proceedings of the American Chemical Society*. Washington, USA: American Chemical Society, 1989.
51. Deteresa SJ, Porter RS and Farris RJ. Experimental verification of a microbuckling model for the axial compressive failure of high performance polymer fibres. *J Mater Sci*. 1988; 23: 1886-1894.
52. Drzal LT. The interfacial and compressive properties of polybenzothiazole fibers. Ohio, USA: Air Force Wright Aeronautical Laboratories, 1986.
53. Allen SR. Tensile recoil measurement of compressive strength for polymeric high performance fibres. *J Mater Sci*. 1987; 22: 853-859.
54. Rozenberg BA and Sigalov GM. *Heterophase network polymers: synthesis, characterization and properties*. Portland, USA: Ringgold Inc, 2002.
55. Fidan S, Palazotto A, Tsai CT and Kumar S. Compressive properties of high-performance polymeric fibers. *Compos Sci Technol*. 1993; 49: 291-297.
56. Vlattas C and Galiotis C. Deformation behaviour of liquid crystal polymer fibres: 1. Converting spectroscopic data into mechanical stress-strain curves in tension and compression. *Polymer*. 1994; 35: 2335-2347.
57. Collyer AA. *Liquid crystal polymers: From structures to applications*. Essex, England: Elsevier, 1992.
58. Technical data sheet of Vectran. In: Inc KA, (ed.). Fort Mill, USA2006.
59. Swolfs Y, Gorbatikh L and Verpoest I. Fibre hybridisation in polymer composites: a review. *Compos Part A Appl Sci Manuf*. 2014; 67: 181-200.
60. Pillai V, Beris AN and Dhurjati P. Intelligent Curing of Thick Composites Using a Knowledge-Based System. *J Compos Mater*. 1997; 31: 22-51.